

PAPER

## High-precision real-time 3D shape measurement based on a quad-camera system

To cite this article: Tianyang Tao *et al* 2018 *J. Opt.* **20** 014009

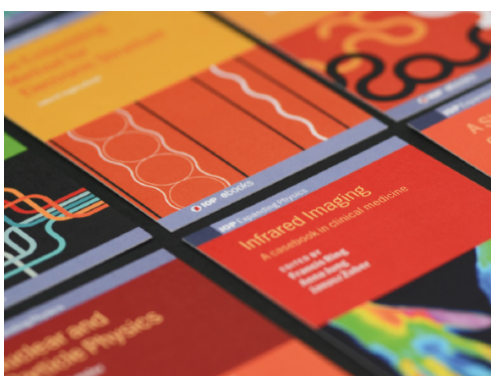
View the [article online](#) for updates and enhancements.

### Related content

- [Real-time microscopic 3D shape measurement based on optimized pulse-width-modulation binary fringe projection](#)
- [Defocusing rectified multi-frequency patterns for high-precision 3D measurement](#)
- [Simplified fringe order correction for absolute phase maps recovered with multiple-spatial-frequency fringe projections](#)

### Recent citations

- [Composite deep learning framework for absolute 3D shape measurement based on single fringe phase retrieval and speckle correlation](#)  
Wei Yin *et al*
- [Dynamic 3D measurement of thermal deformation based on geometric-constrained stereo-matching with a stereo microscopic system](#)  
Yan Hu *et al*



**IOP | ebooks™**

Bringing together innovative digital publishing with leading authors from the global scientific community.

Start exploring the collection—download the first chapter of every title for free.

# High-precision real-time 3D shape measurement based on a quad-camera system

Tianyang Tao<sup>1,2,3</sup> , Qian Chen<sup>1,2</sup>, Shijie Feng<sup>1,2,3</sup>, Yan Hu<sup>1,2,3</sup> ,  
Minliang Zhang<sup>1,2,3</sup> and Chao Zuo<sup>1,2,3,4</sup> 

<sup>1</sup> School of Electronic and Optical Engineering, Nanjing University of Science and Technology, No. 200 Xiaolingwei Street, Nanjing, Jiangsu Province 210094, People's Republic of China

<sup>2</sup> Jiangsu Key Laboratory of Spectral Imaging & Intelligent Sense, Nanjing University of Science and Technology, Nanjing, Jiangsu Province 210094, People's Republic of China

<sup>3</sup> Smart Computational Imaging (SCI) Laboratory, Nanjing University of Science and Technology, Nanjing, Jiangsu Province 210094, People's Republic of China

E-mail: [chenqian@njust.edu.cn](mailto:chenqian@njust.edu.cn) and [surpasszuo@163.com](mailto:surpasszuo@163.com)

Received 15 September 2017, revised 24 November 2017

Accepted for publication 29 November 2017

Published 15 December 2017



CrossMark

## Abstract

Phase-shifting profilometry (PSP) based 3D shape measurement is well established in various applications due to its high accuracy, simple implementation, and robustness to environmental illumination and surface texture. In PSP, higher depth resolution generally requires higher fringe density of projected patterns which, in turn, lead to severe phase ambiguities that must be solved with additional information from phase coding and/or geometric constraints. However, in order to guarantee the reliability of phase unwrapping, available techniques are usually accompanied by increased number of patterns, reduced amplitude of fringe, and complicated post-processing algorithms. In this work, we demonstrate that by using a quad-camera multi-view fringe projection system and carefully arranging the relative spatial positions between the cameras and the projector, it becomes possible to completely eliminate the phase ambiguities in conventional three-step PSP patterns with high-fringe-density without projecting any additional patterns or embedding any auxiliary signals. Benefiting from the position-optimized quad-camera system, stereo phase unwrapping can be efficiently and reliably performed by flexible phase consistency checks. Besides, redundant information of multiple phase consistency checks is fully used through a weighted phase difference scheme to further enhance the reliability of phase unwrapping. This paper explains the 3D measurement principle and the basic design of quad-camera system, and finally demonstrates that in a large measurement volume of 200 mm × 200 mm × 400 mm, the resultant dynamic 3D sensing system can realize real-time 3D reconstruction at 60 frames per second with a depth precision of 50 μm.

Supplementary material for this article is available [online](#)

Keywords: phase-shifting profilometry, real-time 3D, geometric constraints, multi-view system

(Some figures may appear in colour only in the online journal)

## 1. Introduction

Fringe projection profilometry (FPP) [1, 2] has proven to be one of the most promising techniques for the field of 3D

shape measurement due to its non-contact, full-field, and high-resolution nature. Fourier transform profilometry (FTP) [3, 4] and phase-shifting profilometry (PSP) [5, 6] are two main branches of FPP. FTP can reconstruct 3D geometry with a single image, which makes FTP well-suited for dynamic 3D sensing. However, the frequency band overlapping problem

<sup>4</sup> Author to whom any correspondence should be addressed.

limits the measurement precision of FTP. PSP is commonly applied to precisely measuring static objects with multiple images. Compared with FTP, although the measurement efficiency in PSP is reduced, the rapid development of the digital light processing (DLP) technique endows PSP the ability to measure dynamic scenes. In recent years, a number of PSP methods have been proposed to realize real-time 3D shape measurement [6, 7].

Based on the existing DLP technique, the main problem of PSP for measuring the dynamic scenes is motion artifacts. Solutions to this problem can be divided into three categories: reducing the interval between two recording frames, compensating motion artifacts, and improving measurement efficiency (reducing the total number of frames for a single 3D reconstruction). The fringe projection rate of DLP depends on the bit depth of the patterns to be projected. If low-bit (such as 1 bit) patterns are utilized, the projection speed can achieve kHz [8], even tens of kHz [9]. This principle is applied to the defocusing technique [8, 10] to reduce the interval between two adjacent frames, but the problem of defocusing technique is how to design the 1 bit patterns to produce high-quality sinusoidal fringes [11–15]. The second solution is motion artifacts compensation [16, 17], which is a post-processing technique to eliminate motion ripples by estimating the motion displacement and correcting the phase error. To enhance the practicability of this method, computed cost should be reduced, and the accuracy of compensation models still need be improved. Measurement efficiency, the total frames required for a single 3D reconstruction, is the last factor that can be improved to reduce motion artifacts [18, 19]. This paper can be categorized into the third solution, and the related works of this solution are described in following sections.

A large number of additional patterns are required in PSP to eliminate the ambiguities of wrapped phase for measuring complex surfaces [20, 21], which reduces the measurement efficiency and increases the sensitivity to motion artifacts. To increase the efficiency, Liu *et al* [18] proposed a dual-frequency scheme where 3D information can be retrieved from only five composite fringes. The average intensity of the captured fringes for each pixel remains constant during a short period. This property was applied in the bi-frequency scheme to decrease the number of additional fringe patterns [12]. Compared to dual-frequency scheme, there is no reduction of fringe amplitude in bi-frequency scheme. If the fringe amplitude can also be regarded as a constant during a single reconstructed cycle, the number of patterns in bi-frequency scheme can be further reduced to four [19]. Recently, Liu *et al* [22] presented a novel phase-coding scheme using four background and amplitude coded high-frequency fringe patterns. Besides, the phase-coding scheme was introduced to a multi-view system to realize the optimal efficiency (a minimum of three fringe patterns for a single reconstruction) of PSP [23, 24]. All of these methods can realize real-time 3D shape measurement with reduced pattern numbers, but to guarantee the reliability of phase unwrapping, the fringe frequency [12, 18, 19] or fringe amplitude is limited [18, 22–24], which leads to a reduced measurement precision.

In order to increase the measurement efficiency without sacrificing measurement precision, an improved bi-frequency scheme [25] using geometric constraint was proposed where high-precision measurement is realized with five fringe patterns. Geometric constraint, a commonly used technique in passive stereo, was introduced to PSP by [16]. In the work, only three fringe patterns are used for a single 3D reconstruction. This geometry-constraint based technique used in [16] is the so-called stereo phase unwrapping algorithm. Several other techniques using this stereo phase unwrapping algorithm were also presented in [26–29]. All of them can achieve the optimal efficiency of PSP with high precision, but to guarantee the reliability of stereo phase unwrapping, these methods compromise either depth volume [26, 27] or computational cost [28, 29], which leads to a significant reduction of measurement volume or 3D acquisition speed.

Some progress in measurement efficiency has been made in recent years according to previous analyses. Some of the methods can realize real-time measurements, and others can realize high-precision measurements. Whereas many applications require real-time but constantly high-precision measurements. To our knowledge, rare methods can meet these requirements thus an improvement of the classic methods is needed. Measurement efficiency depends on the adopted phase unwrapping algorithm. Stereo phase unwrapping can achieve optimal efficiency but requires a reduction of the measurement precision or 3D acquisition speed to guarantee the robustness. The objective of this work is to develop an improved method of PSP to make high efficiency, high precision and real-time reconstructed performance compatible in a single system. By introducing a quad-camera system and carefully arranging the relative spatial positions between the cameras and the projector, the ambiguities of high-fringe-density wrapped phase are eliminated through flexible phase consistency checks. Robustness of stereo phase unwrapping is enhanced by this technique without the loss of reconstructed precision and speed. The redundant information of phase consistency checks is used by a novel technique called weighted phase difference scheme to further enhance the robustness. Compared with conventional PSP methods, the contributions of this paper are listed as following:

(1) By carefully arranging the relative positions between cameras and the projector, we establish a position-optimized quad-camera system which can reliably eliminate phase ambiguities of high-frequency fringes without projecting any additional patterns or embedding any auxiliary signals or performing any time-consuming algorithms. This position-optimized scheme can also work for  $N$ -camera system, such as dual-camera system, triple-camera system;

(2) The phase differences of phase consistency checks can be fully used by the weighted phase difference scheme to enhance the reliability of stereo phase unwrapping;

(3) The simple algorithm guarantee the large amount of data from four cameras can be processed timely. In a large measurement volume of 200 mm  $\times$  200 mm  $\times$  400 mm, we realize 3D reconstruction at 60 frames per second (fps) with the precision of 50  $\mu$ m.

## 2. Principle

### 2.1. Phase ambiguities in phase shifting profilometry

The classic PSP system consists of one camera and one projector. For an arbitrary point  $(x^C, y^C)$  in the camera space, if we can get its homologous point  $(x^P, y^P)$  in the projector space, the corresponding 3D world coordinates of  $(x^C, y^C)$  can be derived from

$$\begin{aligned} Z(x^C, y^C) &= M^{CP}(x^C, y^C) + \frac{D^{CP}(x^C, y^C)}{J^{CP}(x^C, y^C)x^P + 1}, \\ X(x^C, y^C) &= E^{CP}(x^C, y^C)Z(x^C, y^C) + F^{CP}(x^C, y^C), \\ Y(x^C, y^C) &= G^{CP}(x^C, y^C)Z(x^C, y^C) + H^{CP}(x^C, y^C), \end{aligned} \quad (1)$$

where  $M^{CP}$ ,  $J^{CP}$ ,  $D^{CP}$ ,  $E^{CP}$ ,  $F^{CP}$ ,  $G^{CP}$  and  $H^{CP}$  are related parameter matrices (letters in this paper along with  $(x^C, y^C)$  or other coordinates denote scalar matrix instead of functions) derived from calibration parameters between the camera and the projector [18, 25]. In this paper, superscripts ‘C’ and ‘P’ are added to distinguish between parameters for the camera and projector, whereas superscript ‘CP’ represents common parameters from both camera and projector. Note that either horizontal coordinate  $x^P$  or vertical coordinate  $y^P$  is sufficient enough to retrieve 3D coordinates, and in this paper we use  $x^P$ . To establish the correspondence between  $(x^C, y^C)$  and  $x^P$ , three sinusoidal fringe patterns are projected by the projector and captured by the camera. The intensities of the sinusoidal fringes in  $(x^C, y^C)$  are recorded as

$$\begin{aligned} I_1^C(x^C, y^C) &= A^C(x^C, y^C) + B^C(x^C, y^C)\cos[\Phi^C(x^C, y^C)], \\ I_2^C(x^C, y^C) &= A^C(x^C, y^C) + B^C(x^C, y^C)\cos[\Phi^C(x^C, y^C) \\ &\quad + 2\pi/3], \\ I_3^C(x^C, y^C) &= A^C(x^C, y^C) + B^C(x^C, y^C)\cos[\Phi^C(x^C, y^C) \\ &\quad + 4\pi/3], \end{aligned} \quad (2)$$

where  $A^C$  is average intensity,  $B^C$  is amplitude matrix of fringe, and  $\Phi^C$  is the deformed absolute phase. Using the absolute phase  $\Phi^C$ , an accurate relationship between  $(x^C, y^C)$  and  $x^P$  is established as

$$x^P = \frac{\Phi^C(x^C, y^C)W}{2\pi N}, \quad (3)$$

where  $W$  is the horizontal resolution of the projector, and  $N$  is the total number of fringe periods. However, due to the property of arc-tangent function, only wrapped phase  $\phi^C$  can be directly obtained as following [5]:

$$\begin{aligned} \phi^C(x^C, y^C) &= \arctan \frac{\sqrt{3}[I_1^C(x^C, y^C) - I_3^C(x^C, y^C)]}{[2I_2^C(x^C, y^C) - I_1^C(x^C, y^C) - I_3^C(x^C, y^C)]}. \end{aligned} \quad (4)$$

The relationship between  $\phi^C$  and  $\Phi^C$  can be expressed as

$$\Phi^C(x^C, y^C) = \phi^C(x^C, y^C) + 2k^C(x^C, y^C)\pi, \quad (5)$$

where  $k^C$  is the period order. For each point in the camera, there are  $N$  possibilities for  $k^C$ . This is the so-called phase ambiguities. A large  $N$  can suppress the phase error but

simultaneously increase the phase ambiguities. The basic problem in PSP now becomes how to eliminate this phase ambiguities. The main algorithms to solve this problem include spatial phase unwrapping [30–32], temporal phase unwrapping [33–37] and stereo phase unwrapping [16, 23, 26, 27]. Spatial phase unwrapping is not valid when measuring complex, discontinuous surfaces. On the contrary, temporal phase unwrapping can solve this problem, but requires more recorded images. Stereo phase unwrapping is commonly used in multi-view system to eliminate phase ambiguities since it can measure arbitrary surfaces without additional fringe patterns.

### 2.2. Phase unwrapping using geometry constraint

The main technique of stereo phase unwrapping is geometry constraint. For an arbitrary point  $(x^{C_1}, y^{C_1})$  in camera  $C_1$ , assigning the integers in  $[0, N - 1]$  to  $k^{C_1}(x^{C_1}, y^{C_1})$  one by one,  $N$  corresponding absolute phase  $\Phi_k^{C_1}(x^{C_1}, y^{C_1})$  (to make clearer expression, subscript ‘ $k$ ’ is added in this paper to represent  $k^{C_1}(x^{C_1}, y^{C_1})$ ) and  $N$  corresponding 3D coordinate points (3D candidates) can be obtained. If the measured objects are placed within the depth measurement volume, we can reject some false candidates by applying depth constraint [23, 26, 27]

$$Z_{\min} \leq Z_k(x^{C_1}, y^{C_1}) \leq Z_{\max}, \quad (6)$$

where  $Z_{\min}$  and  $Z_{\max}$  denote the preset depth volume. However, as shown in figure 1(a), it is almost impossible to reject all the false candidates only with depth constraint when  $N$  is large. Setting a large  $Z_{\min}$  and a small  $Z_{\max}$ , or prior-knowledge of the approximate surface geometry [38] can solve the above problem, but both of these two methods are infeasible in most applications. Another solution is embedding code-words into fringes at the cost of reduced fringe amplitude [22] or increased calculation cost [28].

Compared with the above solutions, phase consistency check is a more frequently used technique to eliminate remaining false candidates after depth constraint. An auxiliary camera  $C_2$  is added to the classic PSP system to perform the phase consistency check. The remaining candidates after depth constraint are projected into  $C_2$ , so that we can obtain less than  $N$  corresponding 2D candidates  $(x_k^{C_2}, y_k^{C_2})$ . Theoretically,  $(x^{C_1}, y^{C_1})$  and its homologous point have similar phase. The phase difference  $\Delta\phi_k^{C_1C_2}(x^{C_1}, y^{C_1})$  between  $(x^{C_1}, y^{C_1})$  and the homologous point should satisfy

$$\Delta\phi_k^{C_1C_2}(x^{C_1}, y^{C_1}) = \phi^{C_1}(x^{C_1}, y^{C_1}) - \phi^{C_2}(x_k^{C_2}, y_k^{C_2}) < Thr^{C_2}, \quad (7)$$

where  $\phi^{C_2}(x_k^{C_2}, y_k^{C_2})$  is the wrapped phase of candidate  $(x_k^{C_2}, y_k^{C_2})$ ,  $Thr^{C_2}$  is the preset threshold of phase difference. Note that if  $(x^{C_1}, y^{C_1})$  is a point locating near phase jumping areas ( $\Delta\phi_k^{C_1C_2}(x^{C_1}, y^{C_1}) > 2\pi - Thr^{C_2}$ ), the compensation for  $\Delta\phi_k^{C_1C_2}(x^{C_1}, y^{C_1})$  is performed by

$$\Delta\phi_k^{C_1C_2}(x^{C_1}, y^{C_1}) = 2\pi - \Delta\phi_k^{C_1C_2}(x^{C_1}, y^{C_1}). \quad (8)$$

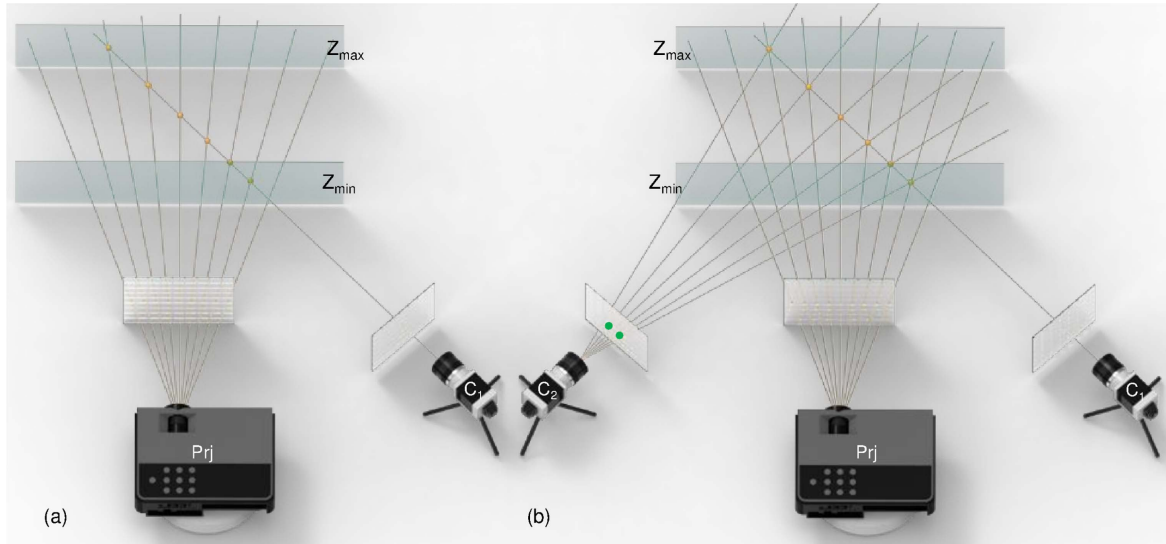


**Figure 1.** The diagram of geometry constraint (the orange points are the 3D candidates). (a) Depth constraint in the classic PSP system; (b) geometry constraint in classic dual-camera system (the green points are the 2D candidates satisfy phase consistency check, and one of these green points is the false candidate).

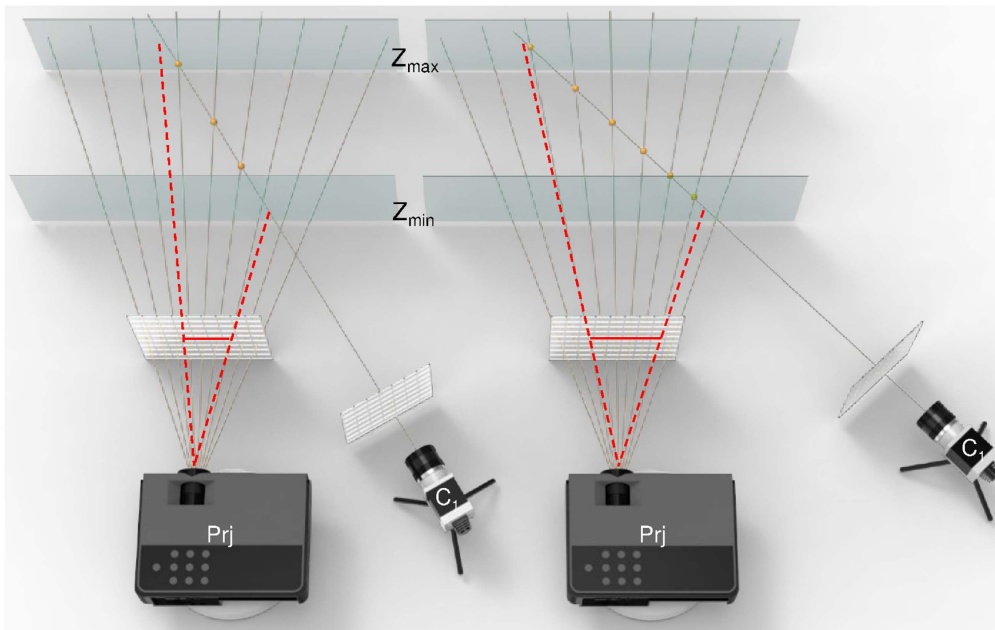


**Figure 2.** The diagram of the effect of baseline on  $N_1(x^{C_1}, y^{C_1})$  (the system in the left has a small baseline and the system in the right has a large baseline).

However, as shown in figure 1(b), some false candidates also satisfy equation (7) when the number of remaining candidates is large enough. To determine the homologous point without reducing the fringe density, additional techniques such as image segmentation and loopy belief propagation are introduced [16, 29, 39]. These post-processing algorithms can enhance the reliability of stereo phase unwrapping even when high-frequency fringes are used, but the additional processing time of these algorithms significantly reduce the performance of real-time 3D reconstruction.

To enhance the reliability of stereo phase unwrapping but constantly guarantee low phase error (large  $N$ ) and the

performance of real-time 3D reconstruction, the only remaining method is performing more phase consistency checks by introducing more additional cameras. This idea is firstly applied to passive stereo [40–42], and has been preliminary adopted in PSP [43]. However, a guided work to design an optimized multi-camera system and the matched algorithm still need be explored for PSP. In this paper, we proposed a quad-camera system to enhance the reliability of stereo phase unwrapping in three aspects: (1) by carefully adjusting the relative spatial positions between cameras and projector, the number of candidates is reduced within the same depth volume; (2) benefiting from the position-optimized quad-camera system, the remaining

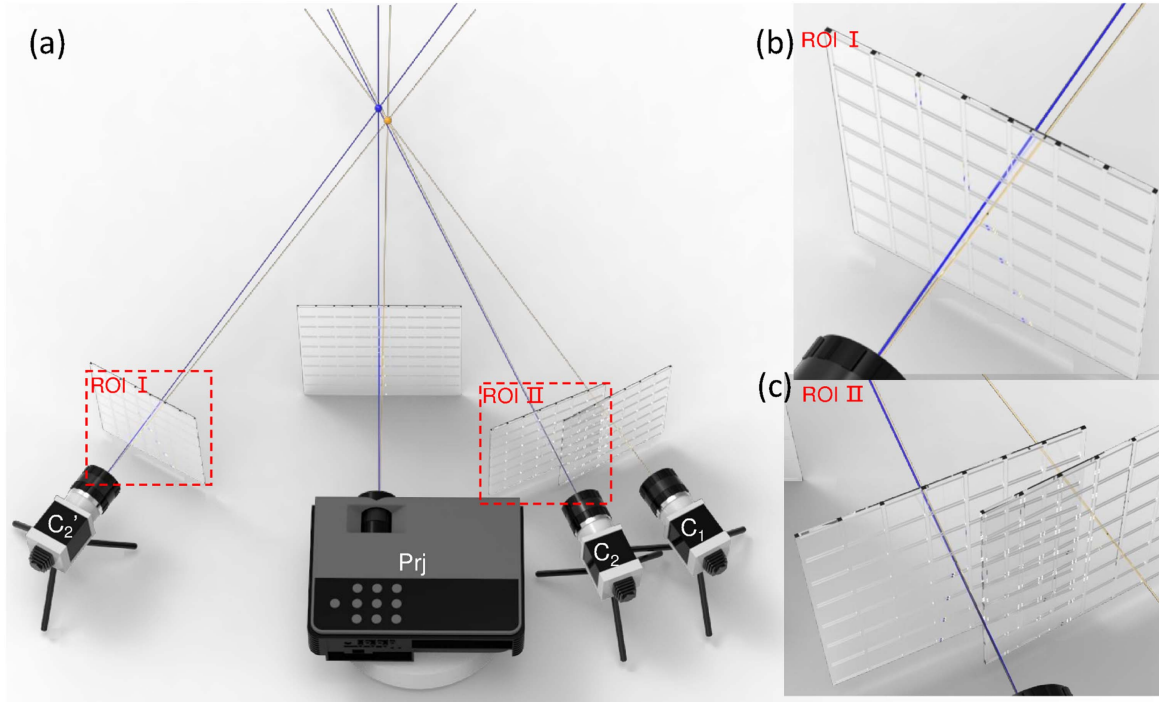


**Figure 3.** The effect of the second auxiliary camera’s position on error reduction of 2D coordinates (the glass plates denote the imaging plane, the orange rays and point denote the ideal rays and 3D candidates, the blue rays and point denote the actual ones). (a) different positions of  $C_2$  in multi-view system; (b) enlarged image of ROI 1; (c) enlarged image of ROI 2.

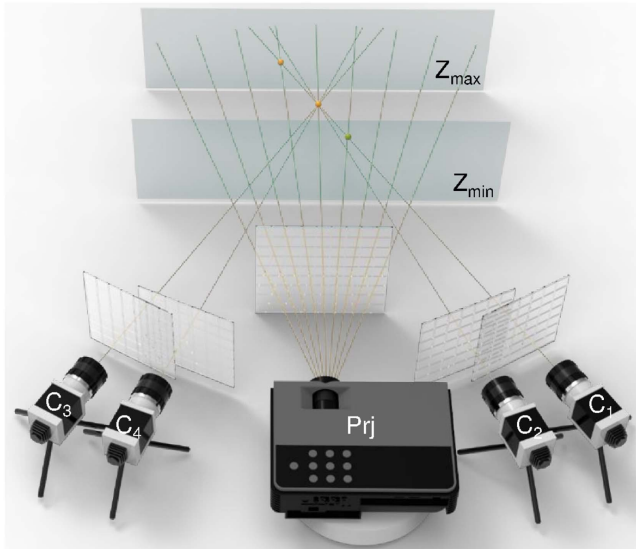


**Figure 4.** The diagram of the position-optimized quad-camera system.

false candidates after depth constraint can be efficiently rejected by multiple phase consistency checks; (3) the redundant information of multiple phase consistency checks is fully used by weighted phase difference scheme to select the final period order. Using this enhanced stereo phase unwrapping, the phase ambiguities can be efficiently eliminated and the absolute phase can be obtained robustly. Then the absolute phase is used to search the homologous point in auxiliary camera to retrieve high-precision 3D geometry.

### 2.3. Optimization design for a quad-camera system

The relative spatial positions between different views in multi-camera system have significant effects on reliability of phase unwrapping. It suggests that to achieve the optimal performance of multi-camera system, each camera must be carefully arranged. In this section, optimization design for relative spatial positions in a quad-camera system is presented.

#### 2.3.1. Optimization design for relative position between the main camera and the projector.

Applying depth constraint, the number of candidates for an arbitrary point  $(x^{C_1}, y^{C_1})$  in the main camera will decrease from  $N$  to  $N_1(x^{C_1}, y^{C_1})$ . A small  $N_1(x^{C_1}, y^{C_1})$  is beneficial to the reliability of stereo phase unwrapping. Setting a small depth volume or reducing the number  $N$  of fringe period is commonly adopted in conventional works, but they come at the price of limited measurement volume and precision, respectively. Thus some other solutions should be explored to achieve a small  $N_1(x^{C_1}, y^{C_1})$ . When the  $Z_{\min}$  and  $Z_{\max}$  are fixed, the value of  $N_1(x^{C_1}, y^{C_1})$  is inversely proportional to the depth distance  $\Delta Z_k(x^{C_1}, y^{C_1})$  between two adjacent candidates. Combining equations (1) and (3) together, we can derive

$$\begin{aligned} \Delta Z_k(x^{C_1}, y^{C_1}) &= |Z_k(x^{C_1}, y^{C_1}) - Z_{k-1}(x^{C_1}, y^{C_1})| \\ &= \left| \frac{D^{C_1P}(x^{C_1}, y^{C_1})C^{C_1P}(x^{C_1}, y^{C_1})}{[C^{C_1P}(x^{C_1}, y^{C_1}) + (C^{C_1P}(x^{C_1}, y^{C_1})x_k^P + 1)N/W](C^{C_1P}(x^{C_1}, y^{C_1})x_k^P + 1)} \right|, \\ x_k^P &= \frac{[\phi(x^{C_1}, y^{C_1}) + 2k(x^{C_1}, y^{C_1})\pi]W}{2\pi N}, \end{aligned} \tag{9}$$

where  $x_k^P$  is the horizontal coordinate in the projector. It can be easily found from equation (9) that  $N_1(x^{C_1}, y^{C_1})$  depends on

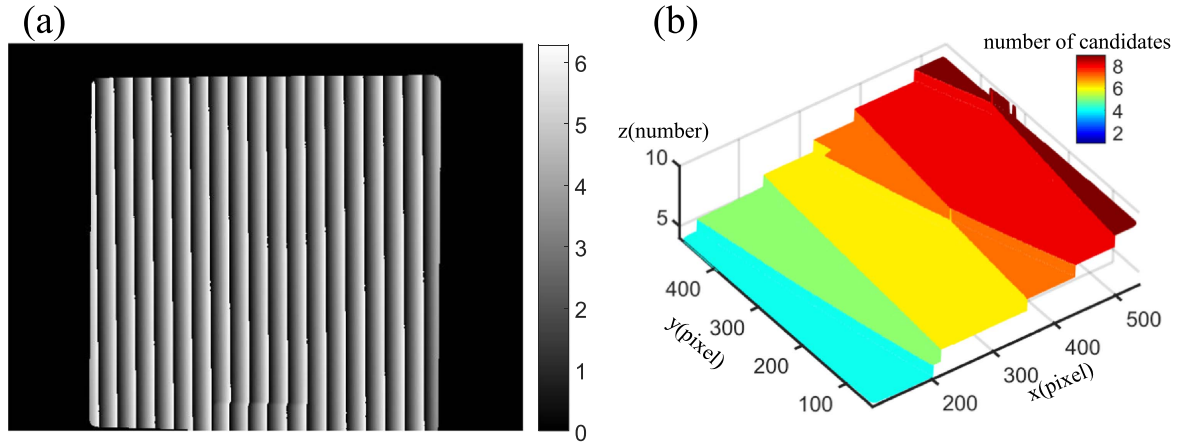


**Figure 5.** The effect of the depth constraint. (a) The wrapped phase map of a plastic plate; (b) distribution of the number of remaining candidates.

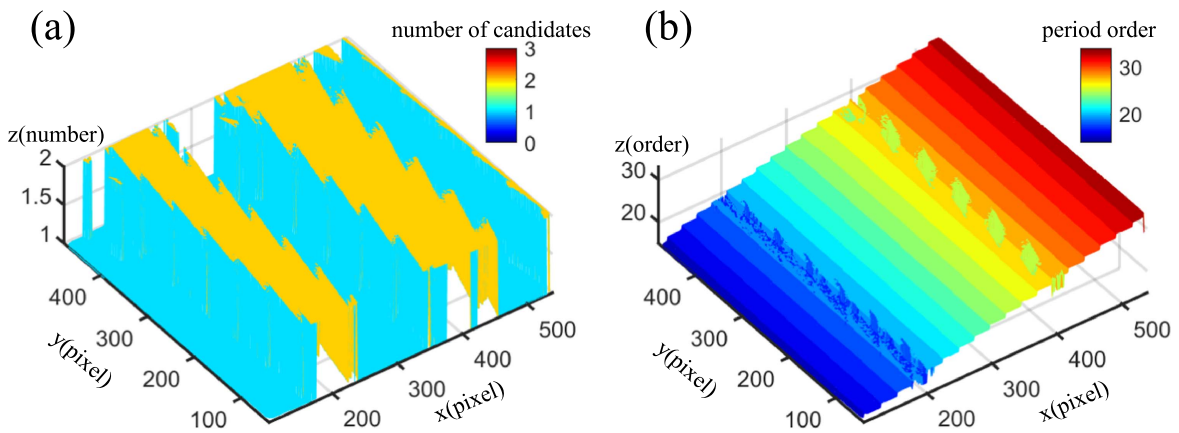


**Figure 6.** The effect of the first phase consistency check. (a) Distribution of the number of remaining candidates; (b) distribution of period orders corresponding to minimum phase difference.

$C^{C_1P}(x^{C_1}, y^{C_1})$ ,  $D^{C_1P}(x^{C_1}, y^{C_1})$  as well as  $N$ . A large  $N$  is required to suppress the phase error, which decreases the  $\Delta Z_k(x^{C_1}, y^{C_1})$ . Then the only remaining way to decrease  $\Delta Z_k(x^{C_1}, y^{C_1})$  is to optimize the parameters  $C^{C_1P}(x^{C_1}, y^{C_1})$  and  $D^{C_1P}(x^{C_1}, y^{C_1})$ . These two parameters are derived from the calibration parameters which are affected by the relative spatial position between the main camera and the projector. Therefore, the optimization of  $C^{C_1P}(x^{C_1}, y^{C_1})$  and  $D^{C_1P}(x^{C_1}, y^{C_1})$  is converted to that of the relative spatial position (baseline and angle). To guarantee a large overlapped field of view (FOV), the baseline and the angle are not the independent variables. The small baseline requires a small angle, and we just replace the relative spatial position with baseline. As shown in figure 2, a small baseline corresponds to a small disparity range (the solid red line) and a large  $\Delta Z_k(x^{C_1}, y^{C_1})$ . By decreasing the baseline between the main camera and the projector, a smaller  $N_1(x^{C_1}, y^{C_1})$  can be obtained through depth constraint.

**2.3.2. Optimization design for relative positions between the main camera and the auxiliary cameras.** The majority of the false candidates are rejected before phase consistency check by depth constraint based on the small baseline camera-projector system. Then an auxiliary camera  $C_2$  is introduced

to this camera-projector system to perform phase consistency check, which is also adopted in conventional multi-view system. The difference is that the position of  $C_2$  is no longer symmetrically arranged on the other side of the projector with the main camera. In previous section, what deserved to be noted is that the small baseline will cause large coordinate errors of the 3D and 2D candidates. As shown in figure 3(a),  $C'_2$  denotes the position of the auxiliary camera in conventional multi-view system. Figure 3(b) displays that a large baseline between  $C_1$  and  $C'_2$  causes considerable coordinate deviation of  $(x_k^{C'_2}, y_k^{C'_2})$ . Therefore, a large  $\text{Thr}^{C_2}$  is required to guarantee the validity of phase consistency check. But it will decrease the efficiency of false candidates rejection, which is adverse to the task of eliminating phase ambiguities. The coordinate errors of 3D candidates are fixed since the baseline between  $C_1$  and projector is fixed. The coordinate errors of 2D candidate  $(x_k^{C_2}, y_k^{C_2})$  depend on the baseline between  $C_2$  and  $C_1$ . A small baseline between  $C_2$  and  $C_1$  will suppress the sensitivity of 2D coordinates to 3D coordinates. Figure 3(a) displays the position of  $C_2$  in our system. Without the loss of overlapped FOV, the small baseline can effectively suppress the errors of  $(x_k^{C_2}, y_k^{C_2})$  (shown in figure 3(c)). Then we can set a small  $\text{Thr}^{C_2}$  to

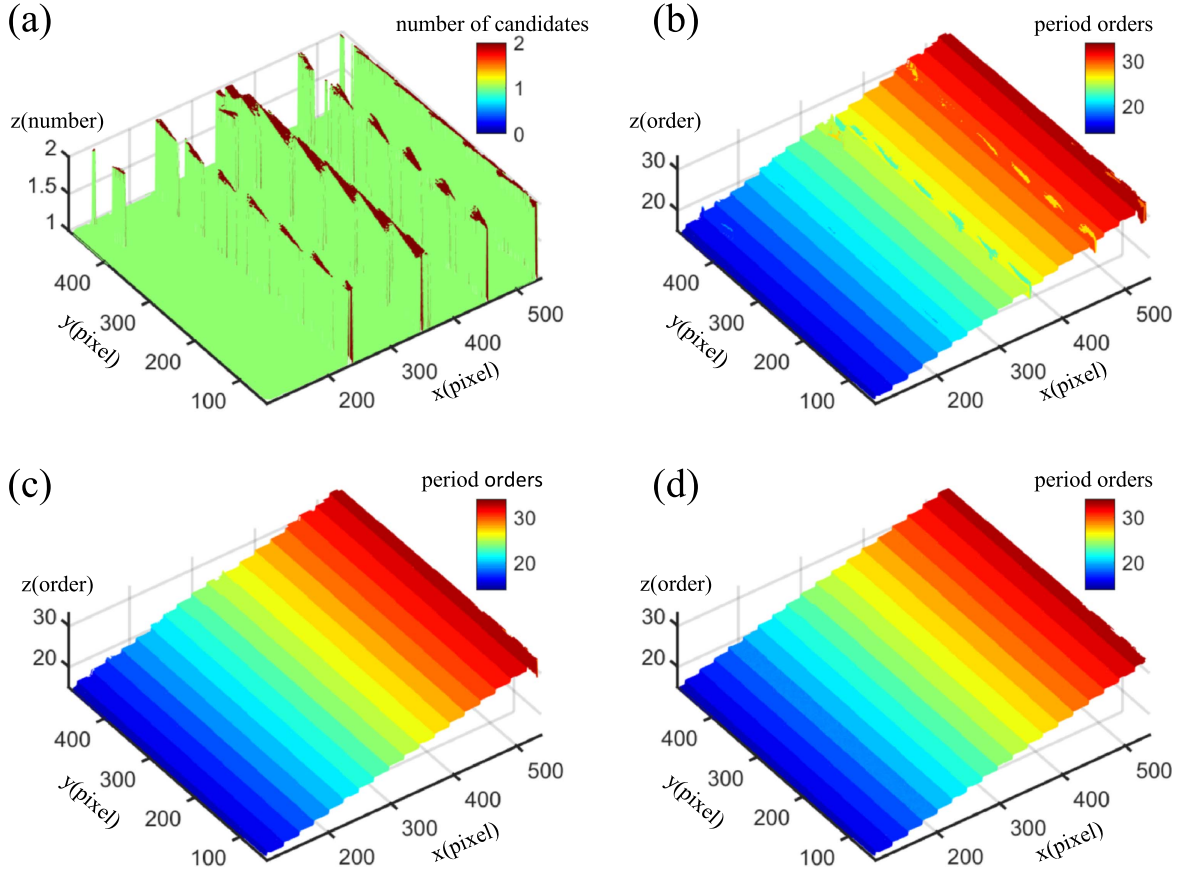


**Figure 7.** The effect of the second phase consistency check. (a) Distribution of the number of remaining candidates; (b) distribution of period orders corresponding to minimum phase difference; (c) distribution of period orders corresponding to minimum sum of weighted phase difference; (d) distribution of period orders after left–right consistency check.

efficiently decrease the number of candidates from  $N_1(x^{C_1}, y^{C_1})$  to  $N_2(x^{C_1}, y^{C_1})$  by phase consistency check. If  $N$  is properly selected,  $N_2(x^{C_1}, y^{C_1})$  will be less than 3, and in most cases  $N_2(x^{C_1}, y^{C_1})$  is 1.

The only candidate remains after depth constraint and phase consistency check for an arbitrary  $P$  in most areas, but further processing (such as another phase consistency check) is still required to eliminate remaining ambiguities of the rest areas. On the other hand, the previous system with small baselines between cameras and projector is not suitable for high-precision 3D reconstruction. Considering these two problems, introducing another auxiliary camera  $C_3$  is reasonable to perform the second phase consistency check and improve the 3D reconstructed precision. Since  $N_2(x^{C_1}, y^{C_1})$  is small enough, decreasing  $N_2(x^{C_1}, y^{C_1})$  is no longer the prior task and the more priority should be shifted to 3D reconstructed precision. According to previous analysis, a large baseline between  $C_3$  and  $C_1$  is necessary to guarantee high-precision 3D reconstruction with a trade-off in  $\text{Thr}^{C_3}$ . Although a large  $\text{Thr}^{C_3}$  decreases the efficiency of the second phase consistency check, it is generally enough to reject all the remaining false candidates of the rest areas.

In multi-camera system, errors of stereo phase unwrapping generally emerge in occluded areas. An efficient method to resolve this problem is left–right consistency check [16, 23, 44]. To guarantee the symmetry of left–right

consistency check, the third auxiliary camera  $C_4$  is introduced to above triple-camera system to establish a quad-camera system. Besides,  $C_4$  can provide another phase consistency check to enhance the reliability of stereo phase unwrapping. The diagram of the quad-camera system is displayed in figure 4.

#### 2.4. Main steps to obtain absolute phase

In section 2.3, we explain the effects of the relative spatial positions between cameras and projector on the reliability of stereo phase unwrapping, and describe how to establish a position-optimized quad-camera system. This section focus on describing the process to obtain the absolute phase.

For an arbitrary point  $(x^{C_1}, y^{C_1})$  in main camera  $C_1$ ,  $N$  3D candidates corresponding to  $k^{C_1}(x^{C_1}, y^{C_1})$  can be obtained by equation (1). The first step to decrease the number of candidates is the depth constraint. In our system,  $N = 48$ ,  $Z_{\min} = -250$  mm and  $Z_{\max} = 150$  mm. Figure 5(b) shows that the number of remaining candidates distributes in [4, 9] after depth constraint. The remaining 3D candidates are then projected into the auxiliary camera  $C_2$  to obtain the corresponding 2D candidates. According to equation (7), the phase differences between each point and its corresponding 2D candidates are calculated and the first phase consistency check is performed to reject the false candidates. Figure 6(a)

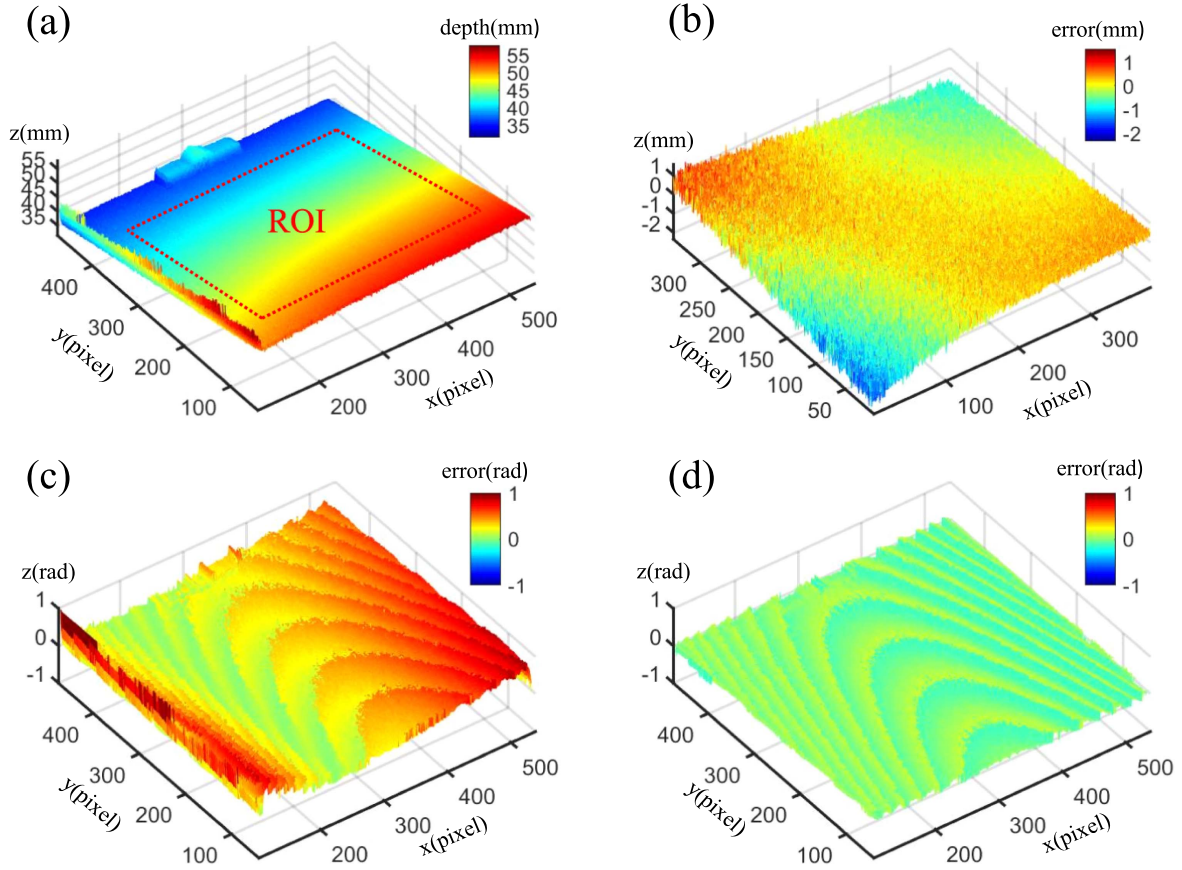


**Figure 8.** The effect of homologous point correction. (a) 3D reconstruction directly from the absolute phase; (b) difference between the measured result and plane fitting result of the region of interest; (c) phase difference  $\Delta\phi^{C_1C_3}(P)$  between  $C_1$  and  $C_3$  before homologous point correction; (d) phase difference  $\Delta\phi^{C_1C_3}(P)$  between  $C_1$  and  $C_3$  after integer homologous point correction.

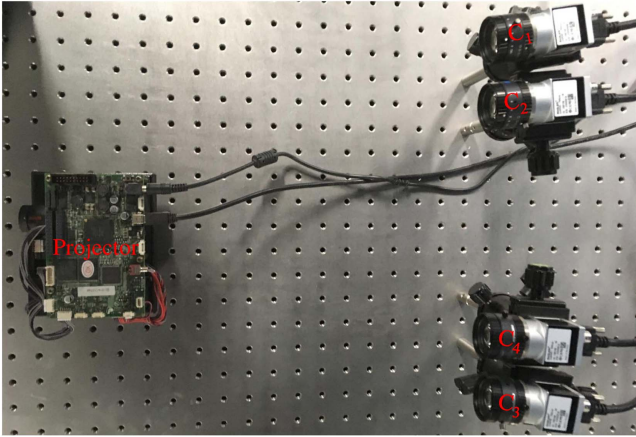


**Figure 9.** The set-up of the quad-camera system.

displays the results after the first phase consistency check with  $\text{Thr}^{C_2} = 0.6$ . We can find that the number of remaining candidates is less than 3 for an arbitrary point in  $C_1$ . Figure 6(b) denotes the period orders corresponding to the minimum phase difference, which indicates that the unreliability of phase unwrapping still exists after the first phase consistency check. To reduce this unreliability, the rest candidates are projected into  $C_3$  to perform the second phase

consistency check with a large threshold  $\text{Thr}^{C_3} = 1.0$ , the related results are shown in figure 7(a). Figure 7(b) indicates that reliability of stereo phase unwrapping increases but the rest errors are still negligible. Actually, the redundancy of the phase differences of two phase consistency checks is not used, and this redundancy is useful for enhancing reliability of stereo phase unwrapping. Using this redundancy, we propose a weighted phase difference scheme to search the homologous point from remaining candidates after the second phase consistency check. By

$$\Delta\phi_k^{C_1C_2C_3}(x^{C_1}, y^{C_1}) = \Delta\phi_k^{C_1C_2}(x_k^{C_2}, y_k^{C_2}) + r^{C_3}\Delta\phi_k^{C_1C_3}(x_k^{C_3}, y_k^{C_3}), \quad (10)$$

the sum of phase differences ( $\Delta\phi_k^{C_1C_2C_3}(x^{C_1}, y^{C_1})$ ) of two phase consistency checks is calculated, where  $r^{C_3}$  is the weighted coefficient,  $\Delta\phi_k^{C_1C_3}(x_k^{C_3}, y_k^{C_3})$  is the phase difference between  $P$  and its 2D candidate in  $C_3$ . The value of weighted coefficient depends on the baseline between the auxiliary camera and the main camera, and the large baseline corresponds to a small weighted coefficient. In this paper, we simply set  $r^{C_3} = 0.6$ . Figure 7(c) displays the effect of weighted phase difference scheme. Compared with figure 7(b), almost all the points can search the correct period order except minor points at the edge of the plate.

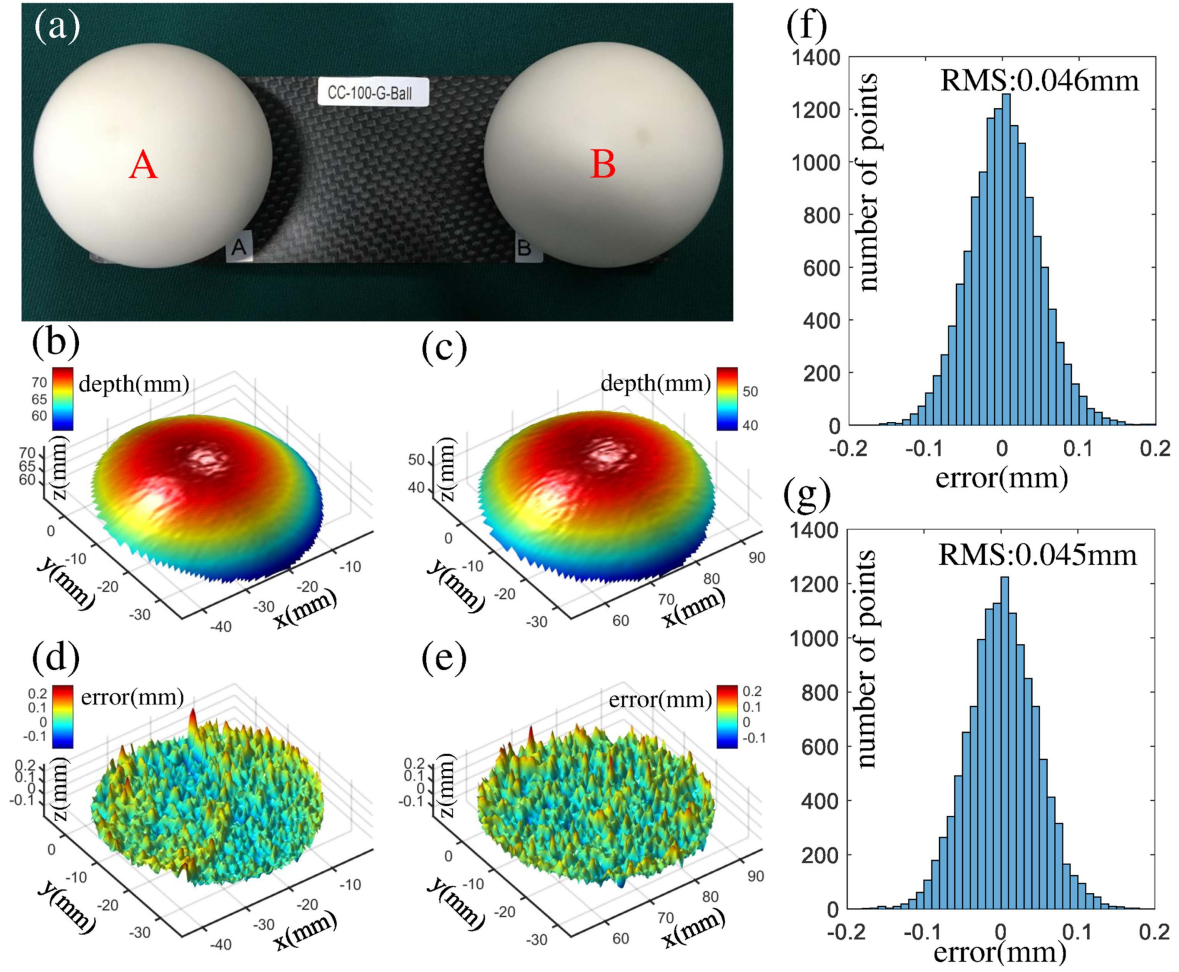


**Figure 10.** Precision analysis for measuring spheres. (a) the ceramic spheres to be measured; (b) the 3D reconstruction results of the sphere A in (a); (c) the 3D reconstruction results of the sphere B in (a); (d) the distribution of the errors of (b); (e) the distribution of the errors of (c); (f) the histogram of (d); (g) the histogram of (e).

The third auxiliary camera  $C_4$  is applied to left–right consistency check to eliminate the minor errors at the edge or occluded areas of the measured surface. Besides,  $C_4$  can provide another phase consistency check, and equation (10) can be updated as

$$\Delta\phi_k^{C_1C_2C_3C_4}(x^{C_1}, y^{C_1}) = \Delta\phi^{C_1C_2}(x_k^{C_2}, y_k^{C_2}) + r^{C_3}\Delta\phi^{C_1C_3}(x_k^{C_3}, y_k^{C_3}) + r^{C_4}\Delta\phi^{C_1C_4}(x_k^{C_4}, y_k^{C_4}), \quad (11)$$

where  $\Delta\phi_k^{C_1C_2C_3C_4}(x^{C_1}, y^{C_1})$  is the sum of the phase differences of three phase consistency checks,  $\Delta\phi^{C_1C_4}(x_k^{C_4}, y_k^{C_4})$  is the phase difference between  $P$  and its 2D candidate in  $C_4$ , and  $r^{C_4} = 0.8$  is the weighted coefficient. The final distribution of period orders after left–right consistency check is shown in figure 7(d), from which we can find the minor errors at the edge of the plate in figure 7(c) are eliminated. After obtaining the period orders, the corresponding absolute phase as well as the 3D coordinates can be derived from equations (5) and (1), respectively.

### 2.5. Homologous point optimization

The analysis in section 2.3 suggests that the 3D geometry retrieved directly from the absolute phase has low precision, which is also indicated in figure 8(b). To improve the 3D reconstructed precision,  $C_1$  and  $C_3$  are used in this paper to reconstruct the 3D results due to the large baseline, but the sub-pixel homologous points are required.

If  $k^{C_1}(x^{C_1}, y^{C_1}) = h$  is the correct period order for point  $(x^{C_1}, y^{C_1})$ , we can use the absolute phase  $\Phi_h^{C_1}(x^{C_1}, y^{C_1})$  to map the homologous point  $(x_h^{C_3}, y_h^{C_3})$ . But this directly obtained homologous point  $(x_h^{C_3}, y_h^{C_3})$  has an offset to the ideal one  $(x_{ide}^{C_3}, y_{ide}^{C_3})$ . The phase difference  $\Delta\phi_h^{C_1C_3}(x^{C_1}, y^{C_1})$  between  $(x^{C_1}, y^{C_1})$  and  $(x_h^{C_3}, y_h^{C_3})$  can be used to denote the offset between  $(x_h^{C_3}, y_h^{C_3})$  and  $(x_{ide}^{C_3}, y_{ide}^{C_3})$ , and the distribution of the difference is shown in figure 8(c). In this paper, only horizontal coordinate of homologous point is used to retrieve 3D information. On the other hand, the error of vertical coordinate is small enough to be neglected. Therefore, only horizontal coordinate needs correction. To eliminate this offset, pixel correction is performed in this paper. Firstly, searching a

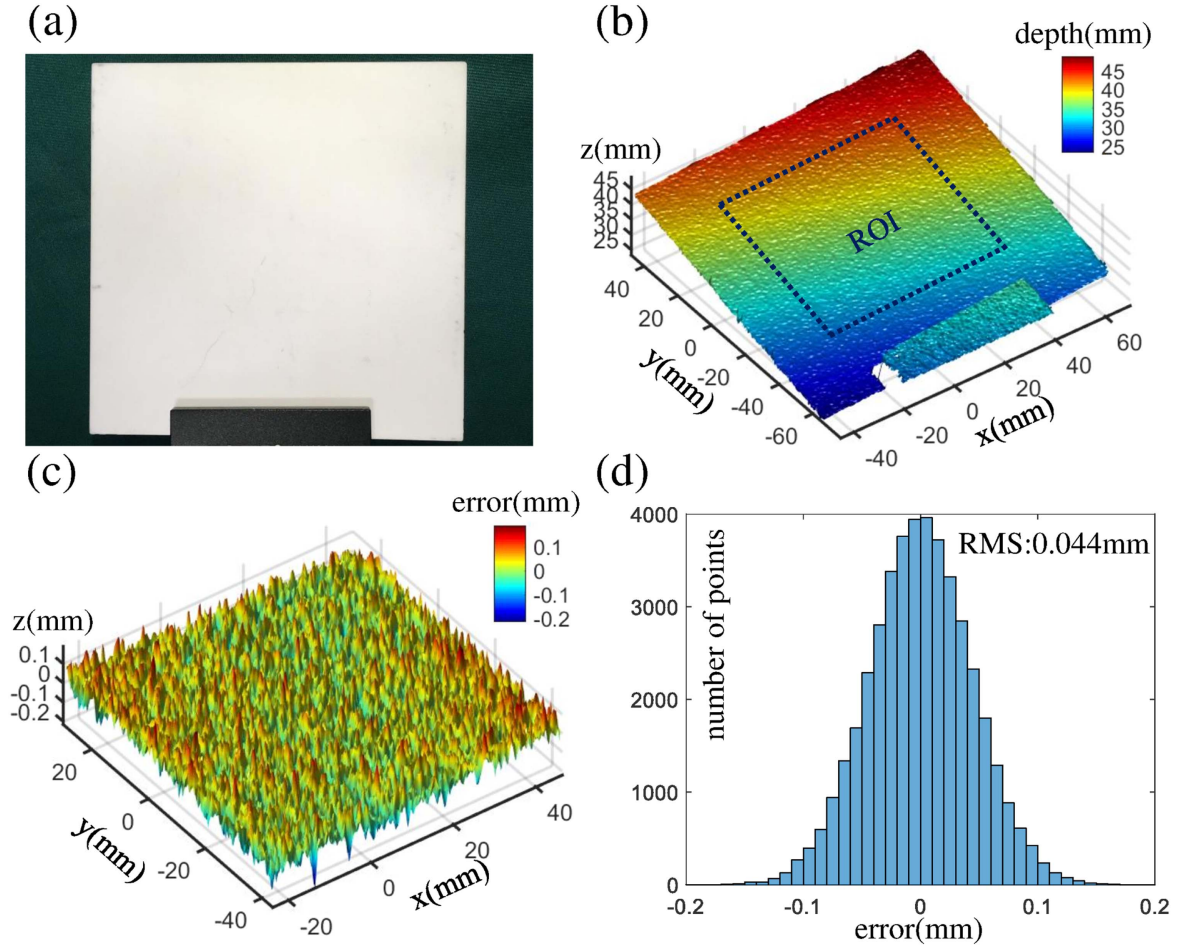


**Figure 11.** Precision analysis for measuring the plane. (a) The ceramic plate to be measured; (b) the 3D reconstruction results of the plate; (c) the distribution of the errors of (b); (d) the histogram of (c).

integer offset  $i$  through

$$\begin{aligned} \Delta\phi_h^{C_1C_3}(x^{C_1}, y^{C_1}) &= \phi^{C_1}(x^{C_1}, y^{C_1}) \\ & - \phi_h^{C_3}(x_h^{C_3} + i, y_h^{C_3}), i \in [-3, 3] \end{aligned} \quad (12)$$

to make  $\Delta\phi_h^{C_1C_3}(x_h^{C_3}, y_h^{C_3})$  minimum, we can eliminate the integer offset and obtain the corrected homologous point  $x_{int}^{C_3} = x_h^{C_3} + i$ . The distribution of  $\Delta\phi_h^{C_1C_3}(x^{C_1}, y^{C_1})$  after integer pixel correction is shown in figure 8(d). Secondly, suppose the variety of the phase is linear, then we can eliminate the sub-pixel offset by

$$x_{sub}^{C_3} = x_{int}^{C_3} + \begin{cases} \frac{\phi^{C_1}(x^{C_1}, y^{C_1}) - \phi_h^{C_3}(x_{int}^{C_3}, y_h^{C_3})}{\phi^{C_3}(x_{int}^{C_3} + 1, y_h^{C_3}) - \phi^{C_3}(x_{int}^{C_3}, y_h^{C_3})}, \\ \phi^{C_1}(x^{C_1}, y^{C_1}) - \phi_h^{C_3}(x_{int}^{C_3}, y_h^{C_3}) > 0 \\ \frac{\phi^{C_1}(x^{C_1}, y^{C_1}) - \phi_h^{C_3}(x_{int}^{C_3}, y_h^{C_3})}{\phi^{C_3}(x_{int}^{C_3}, y_h^{C_3}) - \phi^{C_3}(x_{int}^{C_3} - 1, y_h^{C_3})}, \\ \phi^{C_1}(x^{C_1}, y^{C_1}) - \phi_h^{C_3}(x_{int}^{C_3}, y_h^{C_3}) < 0 \end{cases}, \quad (13)$$

and then we can obtain sub-pixel homologous point  $x_{sub}^{C_3}$ . This pixel correction scheme [45] can guarantee the high precision of the homologous point without time-consuming calculations.

### 3. Experiment

A quad-camera system is developed to verify the feasibility of the proposed method, as shown in figure 9. This set-up includes a LightCrafter 4500 (1140 × 912 resolution), four basler acA-750 μm cameras (640 × 750 resolution, 751 maximum fps), a HP Z230 computer (Intel Xeon E3-1226 v3 CPU, NVIDIA Quadro K2200 GPU). Three phase-shifting fringe patterns are projected into the measured object by LightCrafter at the speed of 100 HZ, and the trigger signals are simultaneously sent to cameras to synchronously capture the deformed fringes, then the captured fringes are processed by the computer. The basic parameter settings include  $Z_{min} = -250$  mm,  $Z_{max} = 150$  mm,  $\text{Thr}^{C_2} = 0.6$  rad,  $\text{Thr}^{C_3} = 1.0$  rad, and  $\text{Thr}^{C_4} = 0.8$  rad,  $r^{C_3} = 0.6$ , and  $r^{C_4} = 0.8$ . Based on these settings, the following experiments are performed to verify the measurement precision, reliability, and speed.

#### 3.1. Precision analysis

To test the precision our system can achieve, we measured a pair of standard ceramic spheres and a standard ceramic plate. The ceramic spheres shown in figure 10(a) have the diameter

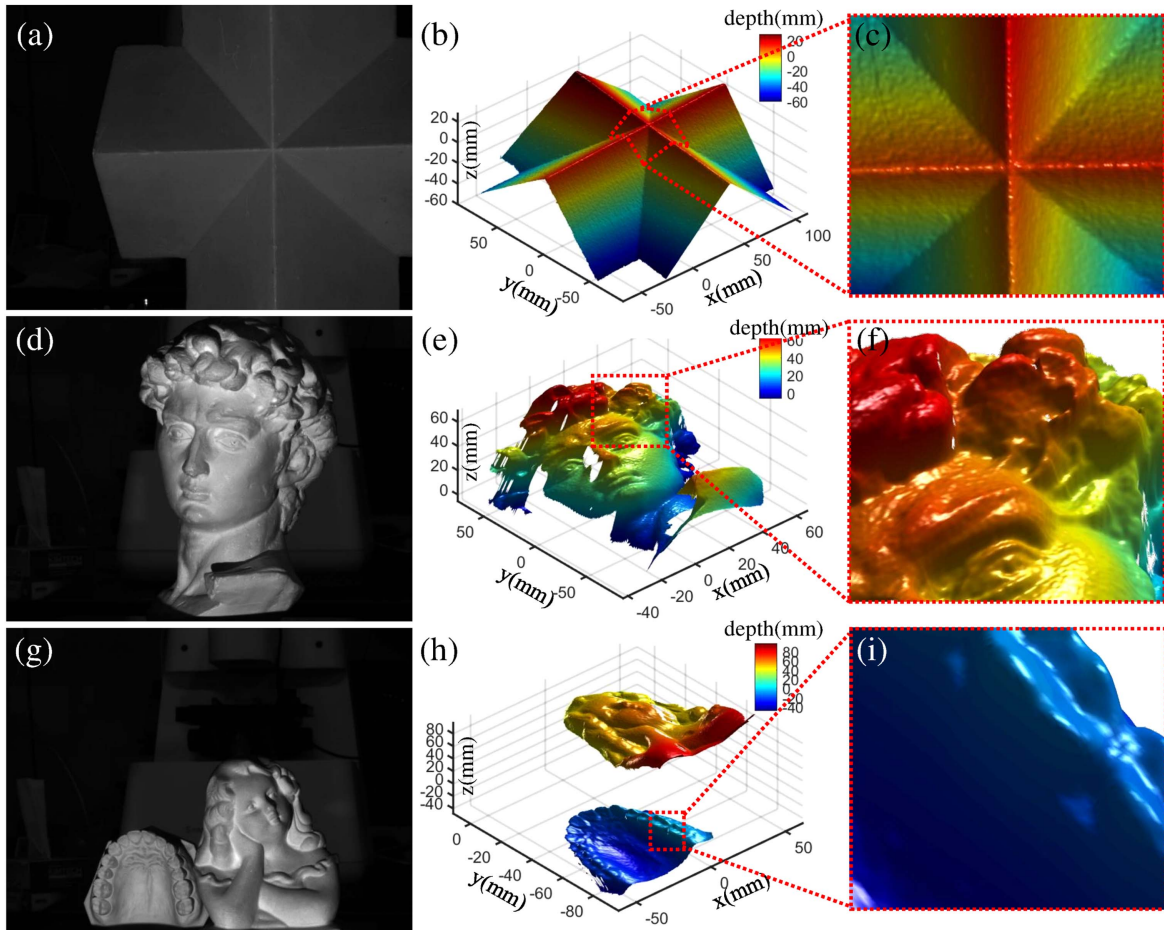


**Figure 12.** Measurement results of special surfaces. (a) The cross prism with a sharp-edged surface; (b) the 3D reconstruction results of (a); (c) the enlarged detail of the region in (b); (d) the David statue with a complex surface; (e) the 3D reconstruction results of (d); (f) the enlarged detail of the region in (e); (g) a tooth model and a girl statue with discontinuous surfaces; (h) the 3D reconstruction results of (g); (i) the enlarged detail of the region in (h).

**Table 1.** Accuracy results of the proposed method.

Measured objects	Correctness			Number of points
	(%)	Error(%)	Miss(%)	
Cross prism	98.02	0.63	1.35	211170
David statue	95.14	1.55	3.31	94423
Isolated objects	96.21	1.26	2.53	70820

of 50.8 mm, micron-sized manufacturing error. Figures 10(b) and (c) display the related 3D reconstruction results. To obtain the measured errors, we perform the spherical fitting using the data in figures 10(b) and (c), then the fitted spheres are set as the ground truth. The differences between the measured data and the ground truth are shown in figures 10(d) and (e). In figures 10(f) and (g), we display the quantitative histograms of figures 10(d) and (e). It can be easily found that the major measured errors of two spheres are less than 100 μm with the rms of 46 μm and 44 μm, respectively. Besides the measurement of curved surface, the plane measurement is also performed with a ceramic plate shown in figure 11(a). Figure 11(b) is the 3D reconstruction results. Figure 11(c) shows the differences between measured data

and the ground truth obtained from plane fitting, and figure 11(d) shows the histogram of figure 11(c). The measured errors of ceramic plate also validate the measurement precision of 50 μm.

### 3.2. Reliability analysis

High-frequency fringes are used to suppress phase error and further improve the 3D reconstructed precision, but the robustness of phase unwrapping is decreased. As 48-period phase-shifting fringes are adopted in our system, some experiments need to demonstrate the reliability of proposed method. Measuring ridged, complex or discontinuous surface is a challenging task for PSP with minimum phase-shifting image number. Therefore, to test the reliability of our system when scanning these challenging surfaces, we measured a cross prism shown in figure 12(a), a David statue shown in figure 12(d) and two isolated objects shown in figure 12(g). Figures 12(b), (e) and (h) display the 3D reconstruction results corresponding to figures 12(a), (d) and (g), and the corresponding enlarged details are shown in figures 12(c), (f) and (i). In order to quantitatively analyze the

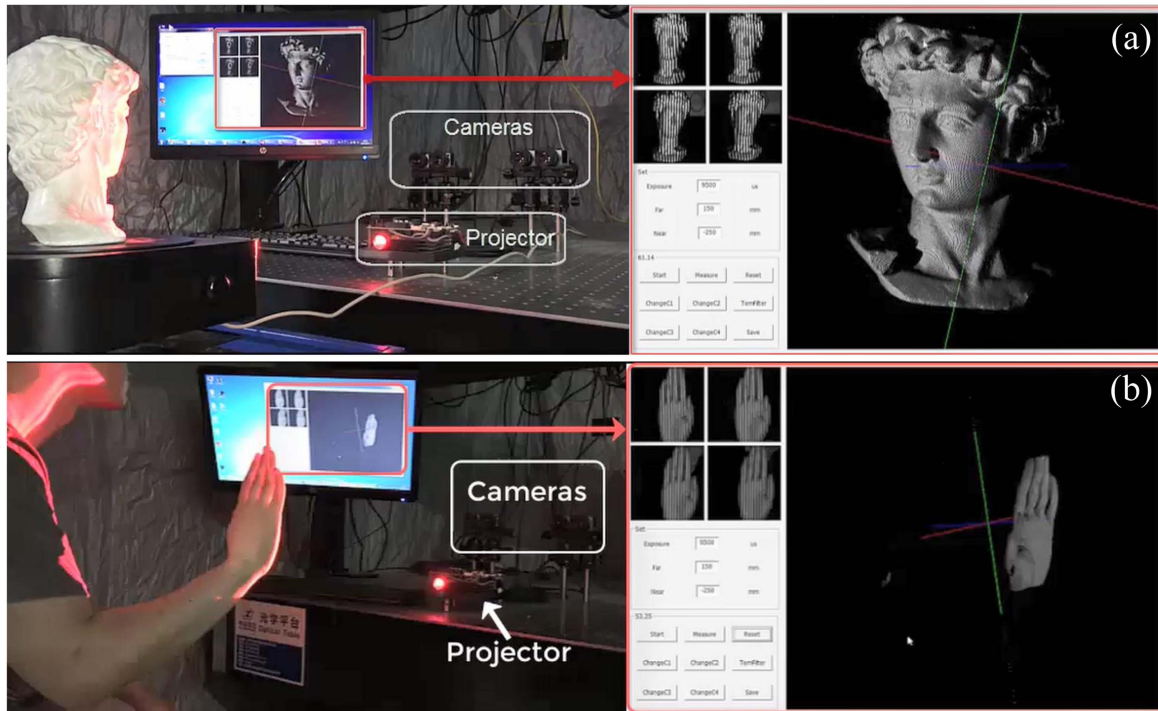


**Figure 13.** Measurement results of dynamic scenes. (a) A frame intercepted from Visualization 1 (see Visualization 1 for more details); (b) a frame intercepted from Visualization 2 (see Visualization 2 for more details).

robustness of our method, the correctness of absolute phase of the above three surfaces is calculated and shown in table 1. The reference phase of these three surfaces are provided by multi-frequency PSP. In table 1, note that the number of points counts all the points with the proper fringe amplitude, and this number is the same value in both methods; the correctness is the percentage of the points having the correct absolute phase; the error is the percentage of the points having the false absolute phase; finally, the miss denotes the percentage of the points without absolute phase, and these points are usually located in occluded areas. We can find from table 1 that even when measuring these challenging surfaces, the correctness percentage still holds at a high level, which demonstrates the reliability of our enhanced stereo phase unwrapping.

### 3.3. Real-time measurement performance

Since no complicated spatial algorithm is included in our method, all the algorithms we have used can be implemented on the GPU, which improves the real-time reconstructed performance. To demonstrate the feasibility of dynamic scenes measurement, we measured a rotating statue of David and a moving hand, respectively. The experiment system acquired a time series of deformed fringe patterns at a rate of 100 HZ with a trigger signal. In the first experiment, a statue of David was rotated by an electro-control turntable, as shown in the left of figure 13(a). The red block diagram in figure 13(a) displays the captured images of four cameras and the reconstructed 3D results. During the measurement process, we zoomed in and rotated the 3D results to show the reconstructed details. The whole measurement process and the related 3D results can be

referred to in Visualization 1 is (available online at [stacks.iop.org/JOPT/20/014009/mmedia](http://stacks.iop.org/JOPT/20/014009/mmedia)). The second experiment can be divided into two parts. In the first part, the hand alternatively opened and closed, carrying on a different movement mode compared with the first experiment. Then the hand moved along the depth direction for a long distance, and this second part is presented to verify that our system has a large measurement volume along the depth direction. The whole measurement process and the related 3D results can be referred to in Visualization 2.

## 4. Conclusions

This paper proposes an enhanced stereo phase unwrapping method with which the optimal efficiency, high precision and the real-time reconstructed performance are compatible in a single system. The relative spatial positions between cameras and projector can be carefully adjusted to enhance the reliability of stereo phase unwrapping. Based on this position-optimized quad-camera system, the phase can be unwrapped by several flexible phase consistency checks and sum of weighted phase difference. This paper uses a quad-camera system to explain the principle and execute the experiments, and if more or less cameras are used in a multi-view system, this position optimization principle is still valid. For the dual-camera case, an asymmetrical system is the prior selection [29]; for the triple-camera case, we can set the third camera near the main camera; note that for the quad-camera case, the fourth camera can also be placed near main camera to further enhance the reliability of phase unwrapping but with some

trade-off in public FOV as well as the performance of left-right consistency check.

However, the parameter settings in this paper are not rigorous. The phase difference thresholds as well as the weighted coefficients are simply set according to the relative positions of cameras since the quantitative relationships are difficult to be established. On the other hand, the 3D geometry is retrieved from main camera C1, but it can also be retrieved from C4 if we set C4 as the main camera. That means more than one 3D geometry can be obtained within a single measurement cycle. Can the redundant information of these 3D geometries from different cameras be utilized to further improve the reconstructed precision? Dealing with these detailed problems deserves future effort.

## Acknowledgments

This work was supported by the National Key Technologies R&D Program of China (2017YFF0106403), National Natural Science Fund of China (61722506, 61705105, 111574152), Final Assembly '13th Five-Year Plan' Advanced Research Project of China (30102070102), Outstanding Youth Foundation of Jiangsu Province of China (BK20170034), National Defense Science and Technology Foundation of China (0106173), 'Six Talent Peaks' project of Jiangsu Province, China (2015-DZXX-009), '333 Engineering' Research Project of Jiangsu Province, China (BRA2016407), Fundamental Research Funds for the Central Universities (30917011204, 30916011322), Open Research Fund of Jiangsu Key Laboratory of Spectral Imaging & Intelligent Sense (3091601410414), China Postdoctoral Science Foundation (2017M621747), and Jiangsu Planned Projects for Postdoctoral Research Funds (1701038A).

## ORCID iDs

Tianyang Tao  <https://orcid.org/0000-0003-1122-5785>

Yan Hu  <https://orcid.org/0000-0003-1558-1541>

Chao Zuo  <https://orcid.org/0000-0002-1461-0032>

## References

- [1] Gorthi S S and Rastogi P 2010 Fringe projection techniques: whither we are? *Opt. Lasers Eng.* **48** 133–40
- [2] Zhang Z 2012 Review of single-shot 3D shape measurement by phase calculation-based fringe projection techniques *Opt. Lasers Eng.* **50** 1097–106
- [3] Takeda M and Mutoh K 1983 Fourier transform profilometry for the automatic measurement of 3-D object shapes *Appl. Opt.* **22** 3977–82
- [4] Su X and Zhang Q 2010 Dynamic 3-D shape measurement method: a review *Opt. Lasers Eng.* **48** 191–204
- [5] Srinivasan V, Liu H-C and Halioua M 1984 Automated phase-measuring profilometry of 3-D diffuse objects *Appl. Opt.* **23** 3105–8
- [6] Zhang S 2010 Recent progresses on real-time 3D shape measurement using digital fringe projection techniques *Opt. Lasers Eng.* **48** 149–58
- [7] Van der Jeught S and Dirckx J J 2016 Real-time structured light profilometry: a review *Opt. Lasers Eng.* **87** 18–31
- [8] Lei S and Zhang S 2009 Flexible 3-D shape measurement using projector defocusing *Opt. Lett.* **34** 3080–2
- [9] Zuo C, Tao T, Feng S, Huang L, Asundi A and Chen Q 2017 Micro Fourier transform profilometry ( $\mu$ FTP): 3D shape measurement at 10,000 frames per second *Opt. Lasers Eng.* **102** 70–91
- [10] Zhang S, Van Der Weide D and Oliver J 2010 Superfast phase-shifting method for 3-D shape measurement *Opt. Express* **18** 9684–9
- [11] Wang Y and Zhang S 2011 Superfast multifrequency phase-shifting technique with optimal pulse width modulation *Opt. Express* **19** 5149–55
- [12] Zuo C, Chen Q, Gu G, Feng S, Feng F, Li R and Shen G 2013 High-speed three-dimensional shape measurement for dynamic scenes using bi-frequency tripolar pulse-width-modulation fringe projection *Opt. Lasers Eng.* **51** 953–60
- [13] Xu Y, Ekstrand L, Dai J and Zhang S 2011 Phase error compensation for three-dimensional shape measurement with projector defocusing *Appl. Opt.* **50** 2572–81
- [14] Zhao H, Diao X, Jiang H and Li X 2017 High-speed triangular pattern phase-shifting 3D measurement based on the motion blur method *Opt. Express* **25** 9171–85
- [15] Hu Y, Chen Q, Feng S, Tao T, Li H and Zuo C 2017 Real-time microscopic 3-D shape measurement based on optimized pulse-width-modulation binary fringe projection *Meas. Sci. Technol.* **28** 075010
- [16] Weise T, Leibe B and Gool L Van 2007 Fast 3D scanning with automatic motion compensation *IEEE Conf. on Computer Vision and Pattern Recognition, 2007. CVPR'07* (Piscataway, NJ: IEEE) pp 1–8
- [17] Lu L, Xi J, Yu Y and Guo Q 2014 Improving the accuracy performance of phase-shifting profilometry for the measurement of objects in motion *Opt. Lett.* **39** 6715–8
- [18] Liu K, Wang Y, Lau D L, Hao Q and Hassebrook L G 2010 Dual-frequency pattern scheme for high-speed 3-D shape measurement *Opt. Express* **18** 5229–44
- [19] Zuo C, Chen Q, Gu G, Feng S and Feng F 2012 High-speed three-dimensional profilometry for multiple objects with complex shapes *Opt. Express* **20** 19493–510
- [20] Sansoni G, Carocci M and Rodella R 1999 Three-dimensional vision based on a combination of gray-code and phase-shift light projection: analysis and compensation of the systematic errors *Appl. Opt.* **38** 6565–73
- [21] Feng S, Zhang Y, Chen Q, Zuo C, Li R and Shen G 2014 General solution for high dynamic range three-dimensional shape measurement using the fringe projection technique *Opt. Lasers Eng.* **59** 56–71
- [22] Liu X and Kofman J 2017 Background and amplitude encoded fringe patterns for 3D surface-shape measurement *Opt. Lasers Eng.* **94** 63–9
- [23] Tao T, Chen Q, Da J, Feng S, Hu Y and Zuo C 2016 Real-time 3-D shape measurement with composite phase-shifting fringes and multi-view system *Opt. Express* **24** 20253–69
- [24] Lohry W and Zhang S 2014 High-speed absolute three-dimensional shape measurement using three binary dithered patterns *Opt. Express* **22** 26752–62
- [25] Tao T, Chen Q, Feng S, Hu Y, Da J and Zuo C 2017 High-precision real-time 3D shape measurement using a bi-frequency scheme and multi-view system *Appl. Opt.* **56** 3646–53
- [26] Bräuer-Burchardt C, Munkelt C, Heinze M, Kühmstedt P and Notni G 2011 Using geometric constraints to solve the point correspondence problem in fringe projection based 3D measuring systems *Image Anal. Process.* **2011** 265–74
- [27] Li Z, Zhong K, Li Y F, Zhou X and Shi Y 2013 Multiview phase shifting: a full-resolution and high-speed 3D measurement framework for arbitrary shape dynamic objects *Opt. Lett.* **38** 1389–91

- [28] Zhang Y, Xiong Z and Wu F 2013 Unambiguous 3D measurement from speckle-embedded fringe *Appl. Opt.* **52** 7797–805
- [29] Breitbartha A, Müllerb E, Kühmstedta P, Notnia G and Denzlerd J 2015 Phase unwrapping of fringe images for dynamic 3D measurements without additional pattern projection *SPIE Sensing Technology+ Applications* (International Society for Optics and Photonics) p 948903
- [30] Goldstein R M, Zebker H A and Werner C L 1988 Satellite radar interferometry: two-dimensional phase unwrapping *Radio Sci.* **23** 713–20
- [31] Flynn T J 1997 Two-dimensional phase unwrapping with minimum weighted discontinuity *J. Opt. Soc. Am. A* **14** 2692–701
- [32] Herráez M A, Burton D R, Lalor M J and Gdeisat M A 2002 Fast two-dimensional phase-unwrapping algorithm based on sorting by reliability following a noncontinuous path *Appl. Opt.* **41** 7437–44
- [33] Huntley J M and Saldner H 1993 Temporal phase-unwrapping algorithm for automated interferogram analysis *Appl. Opt.* **32** 3047–52
- [34] Zhao H, Chen W and Tan Y 1994 Phase-unwrapping algorithm for the measurement of three-dimensional object shapes *Appl. Opt.* **33** 4497–500
- [35] Zhang Z, Towers D P and Towers C E 2010 Snapshot color fringe projection for absolute three-dimensional metrology of video sequences *Appl. Opt.* **49** 5947–53
- [36] Long J, Xi J, Zhang J, Zhu M, Cheng W, Li Z and Shi Y 2016 Recovery of absolute phases for the fringe patterns of three selected wavelengths with improved anti-error capability *J. Mod. Opt.* **63** 1695–705
- [37] Zuo C, Huang L, Zhang M, Chen Q and Asundi A 2016 Temporal phase unwrapping algorithms for fringe projection profilometry: a comparative review *Opt. Lasers Eng.* **85** 84–103
- [38] An Y, Hyun J-S and Zhang S 2016 Pixel-wise absolute phase unwrapping using geometric constraints of structured light system *Opt. Express* **24** 18445–59
- [39] Garcia R R and Zakhora A 2012 Consistent stereo-assisted absolute phase unwrapping methods for structured light systems *IEEE J. Sel. Top. Signal Process.* **6** 411–24
- [40] Okutomi M and Kanade T 1993 A multiple-baseline stereo *IEEE Trans. Pattern Anal. Mach. Intell.* **15** 353–63
- [41] Hartley R and Zisserman A 2003 *Multiple View Geometry in Computer Vision* (Cambridge: Cambridge University Press)
- [42] Furukawa Y and Ponce J 2010 Accurate, dense, and robust multiview stereopsis *IEEE Trans. Pattern Anal. Mach. Intell.* **32** 1362–76
- [43] Guan Y, Yin Y, Li A, Liu X and Peng X 2014 Dynamic 3D imaging based on acousto-optic heterodyne fringe interferometry *Opt. Lett.* **39** 3678–81
- [44] Scharstein D and Szeliski R 2003 High-accuracy stereo depth maps using structured light *IEEE Computer Society Conf. on Computer Vision and Pattern Recognition* vol 1 (Piscataway, NJ: IEEE)
- [45] Song K, Hu S, Wen X and Yan Y 2016 Fast 3D shape measurement using fourier transform profilometry without phase unwrapping *Opt. Lasers Eng.* **84** 74–81